Fluctuations and power-law scaling of dry, frictionless granular rheology near the hard-particle limit

A. P. Santos,[1,*] Ishan Srivastava,[2] Leonardo E. Silbert,[3]
Jeremy B. Lechman,[1,†] and Gary S. Grest[1]
[1]*Sandia National Laboratories, Albuquerque, New Mexico 87185, USA*
[2]*Center for Computational Sciences and Engineering, Lawrence Berkeley National Laboratory, Berkeley, California 94720, USA*
[3]*School of Math, Science and Engineering, Central New Mexico Community College, Albuquerque, New Mexico 87106, USA*

(Received 12 January 2022; accepted 22 July 2022; published 19 August 2022)

The flow of frictionless granular particles is studied with stress-controlled discrete element modeling simulations for systems varying in size from 300 to 100 000 particles. The volume fraction and shear-stress ratio μ are relatively insensitive to system size for a wide range of inertial numbers I. Second-order effects in strain rate, such as normal stress differences, require large system sizes to accurately extract meaningful results, notably a nonmonotonic dependence in the first normal stress difference with strain rate. The rheological response represented by the $\mu(I)$ scalar model works well at describing the lower-order aspects of the rheology, except near the quasistatic limit of these stress-controlled flows. The pressure is varied over five decades, and a pressure dependence of the coordination number is observed, which is not captured by the inertial number. Large fluctuations observed for small systems $N \leqslant 1000$ near the quasistatic limit can lead to the arrest of flow resulting in challenges to fitting the data to rheological relationships. The inertial number is also insufficient for capturing the pressure-dependent behavior of property fluctuations. Fluctuations in the flow and microstructural properties are measured in both the quasistatic and inertial regimes, including shear stress, pressure, strain rate, normal stress differences, volume fraction, coordination number, and contact fabric anisotropy. The fluctuations in flow properties scale self-similarly with pressure and system size. A transition in the scaling of fluctuations of stress properties and contact fabric anisotropy are measured and proposed as a quantitative identification of the transition from inertial to quasistatic flow.

DOI: 10.1103/PhysRevFluids.7.084303

I. INTRODUCTION

Granular particles with frictionless interparticle contacts display an effective macroscopic friction and resistance to flow. Once the material overcomes the yield stress and flows, it dilates and the shear stress increases as the strain rate increases. The $\mu(I)$ rheological model for dense, inertial, steady-state flows of granular materials has emerged as an accurate description of granular rheology [1,2]. The model assumes that in the bulk limit the shear stress τ to pressure P ratio, or shear-stress ratio $\mu = \tau/P$, and the volume fraction ϕ vary monotonically with respect to the

*Present address: AMA Inc., Thermal Protection Materials Branch, NASA Ames Research Center, Moffett Field, CA 94035, USA.
†jblechm@sandia.gov

 ©2022 American Physical Society

dimensionless flow rate inertial number

$$I = \frac{\dot{\gamma}\bar{d}}{2}\sqrt{\frac{\rho_p}{P}}, \tag{1}$$

where $\dot{\gamma}$ is the strain rate, $\bar{d}$ is the average particle diameter, and ρ_p is the density of the particles. The $\mu(I)$ rheology applies quite generally across different flow geometries, including flows down an incline plane [2] and rotating drums [3], and suspension flows where frictional contacts dominate [4]. Naturally, the goal is to develop a robust continuum description that can be used as a predictive tool for a wide variety of natural and technological processes, including scale-up. Further development of such continuum descriptions include wall effects [5], higher-order rheological effects [6], fluctuations, and nonlocal effects [7].

However, the reduction of the shear and strain rate tensors to μ and I, respectively, loses information that is important for distinguishing many rheological behaviors. For example, scalar models such as $\mu(I)$ do not explain anomalous stress profiles in cylindrical Couette flow [8] and negative rod climbing in rotating-rod flow [9]. The lack of coaxiality between principal directions of stress and strain rate tensors in viscometric flows [10–13] contributes to those effects. Srivastava *et al.* [6] developed a second-order rheological model that does not assume coaxiality of stress and strain rate tensors, which is important for capturing the role of interparticle friction on granular rheology. Tensorial expressions of shear and strain rate are also important for describing the influence of loading geometries, as shown by Clemmer *et al.* [14] in irrotational loading geometries of granular flows, where Drucker-Prager-type models [15] can be insufficient. A goal of this paper is to understand the effect of pressure and system size N on the tensorial second-order rheological model [6], without the added contributions due to frictional contacts or suspensions.

In addition to bulk rheological models, nonlocal models have been developed to describe boundary and finite-size effects. Nonlocality can be described as fluctuations in one area of the material inducing change in another area [16] and is often introduced through a granular fluidity field. Fluctuations in microscopic variables, such as the stress [16], strain rate [17], particle velocity [18], and force network fluctuations [19,20], have been used to characterize granular fluidity in nonlocal models. Kinetic theories provide explicit connections between fluctuations and higher-order rheological properties, such as the connection between anisotropy in the second moment of velocity fluctuations and normal stress differences [10,21]. Experiments and simulations have shown that the mean velocity fluctuations scale with the inertial number for a variety of flow geometries [1,22,23] and signal particle friction-dependent flow regimes [24]. The granular temperature [25], defined as the second moment of the velocity, can be used to understand how $\mu(I)$ depends on flow configurations [26]. Going beyond the second moment of the velocity has been used to identify the transition from critical and plastic regimes in granular flows [27]. Transitions in wet granular flow, specifically shear thickening, have been connected to stress fluctuations [28,29]. Another goal of this paper is to present the P and N scaling of fluctuations of flow and microstructural properties.

Because fluctuations play a crucial role in granular rheology, a careful analysis of their scaling properties, particularly with system size N, is crucial. System size is known to affect mean flow properties. For example, Perrin *et al.* experimentally observed that as the height of frictionless granular flows, and thus the number of particles, down an incline increases, the critical stress ratio decreases [30]. Simulations have been used extensively to study system-size and pressure effects in frictionless granular flows. Simulations of two- and three-dimensional particles under stress- and strain-controlled simple shear have fit power laws to $\mu(I)$ and $\phi(I)$ [31–34], among other forms [5,35]. Those fit parameters have power-law dependencies on N and P [31–33], as was also found for shear-jammed systems [36–42]. Fits to data from simulations, experiments, and different configurations have resulted in a range of power-law exponent values [30–32,43–47] that match well with theoretical predictions [47]. Fitting such power laws require large amounts of robust data. In this paper we examine frictionless granular flows for a large range of N, P, and I and study the effect of N and P on tensorial granular rheology [6] and its intrinsic fluctuations.

We present stress-controlled simulations, where flow is induced by applying simple shear to the periodic boundaries of systems with $300 \leqslant N \leqslant 100\,000$ frictionless monodisperse spherical three-dimensional particles and pressures $10^{-6} \leqslant P \leqslant 10^{-2}$. We explore the role of pressure and system size on $\mu(I)$, $\phi(I)$, normal stress differences (in Sec. III A), and rheological fluctuations (in Sec. III B) of steady-state flows.

II. METHODOLOGY

Particles are modeled as spheres of finite size using discrete-element particle-based simulations. The spheres are purely repulsive and only interact when in contact, through a Hookean spring-dashpot interaction potential without friction. Particle diameters d_i are uniformly distributed within $0.9 < d_i < 1.1$ to prevent crystallization. The particles have equal density $\rho_p = 1.91$ and a mean particle mass $\bar{m} = 1$. Some simulations are run with $\rho_p = 1$ for $N = 10^4$ with no observable impact on the measured properties. The particle spring and damping parameters are set to $k_n = 1.0$ and $\gamma_n = 0.5\sqrt{k_n/\bar{m}}$, where the energy scale $k_n\bar{d}^2$ is set by the spring constant and diameter. Particle parameters k_n and γ_n are kept constant and the pressure P is varied. In the absence of gravity, k_n sets the scale of stress. Therefore, varying P and keeping k_n constant is equivalent to varying k_n and keeping P constant [48]. The presented pressure P and stresses σ are nondimensional $P = P'\bar{d}/k_n$, where P' is the dimensional pressure. Campbell [49] found that quasistatic flows are not sensitive to the coefficient of restitution for small strain rates where impact velocities are small. The presented simulation strain rates are in the small regime [49] ($I < 0.5$ for $P = 10^{-3}$) and the results are expected to be insensitive to γ_n. The coefficient of restitution [48] for these simulations is 0.94 (and 0.96 for the simulations $\rho_p = 1$).

The assumption of linear elastic behavior for interparticle contacts is a reasonably accurate model for sufficiently stiff particles at sufficiently low pressure. As an example, glass particles, which have a yield stress $\sigma_y \approx 70$ MPa, would fracture at $P \gg 10^{-3}$ and spherical models would be less appropriate at those high pressures. Even though the particle model does not include particle deformation, simulations are presented for $P \geqslant 10^{-3}$. The higher pressures offer a comparison to previous work.

Simulations are initialized with particles at random nonoverlapping positions and low volume fraction $\phi_0 = 0.05$ in a cubic box with periodic boundary conditions. Initial translational and rotational velocities are set to zero. Flow is induced with a constant stress tensor methodology where the volume fraction and strain rate are not inputs but are measured, distinct from constant volume and constant strain rate simulations [50,51]. The fully periodic three-dimensional box is able to change shape with triclinic deformations to maintain the applied stress tensor [34,52]. The stress-controlled, periodic boundary simulation box models bulk behavior away from walls, thus avoiding wall effects on $\mu(I)$ [5,53,54]. In particular, the Shinoda-Shiga-Mikami [55] formulation of a barostat was used in the $N\mathbf{P}_{\text{ext}}H$ ensemble to integrate the positions and momenta of the particles and box, where N is the number of particles, $\mathbf{P}_{\text{ext}}$ is the applied external pressure tensor, and H is the enthalpy. Stress-controlled simple shear flow is simulated by applying an external stress tensor to the box defined as

$$\boldsymbol{\sigma}_{\text{ext}} = \begin{bmatrix} \sigma_{\text{ext},xx} & \sigma_{\text{ext},xy} & 0 \\ \sigma_{\text{ext},yx} & \sigma_{\text{ext},yy} & 0 \\ 0 & 0 & \sigma_{\text{ext},zz} \end{bmatrix}, \tag{2}$$

where $\sigma_{\text{ext},xx} = \sigma_{\text{ext},yy} = \sigma_{\text{ext},zz} = P_{\text{ext}}$ and the shear stress $\sigma_{\text{ext},xy} = \sigma_{\text{ext},yx} = \tau_{\text{ext}}$, with the other off-diagonal stresses $\sigma_{\text{ext},xz} = \sigma_{\text{ext},yz} = \sigma_{\text{ext},zx} = \sigma_{\text{ext},zy} = 0$. The strain rate tensor $\mathbf{D}$ and the Cauchy stress tensors are measured from the box deformation. Time series of the stress tensor component for select cases, shown in Fig. S1 of the Supplemental Material [56], demonstrate that $|\boldsymbol{\sigma}| = \boldsymbol{\sigma}_{\text{ext}}$, except for the shear stress σ_{xy}. The imbalance between the measured and applied shear stress drives the dynamics of the system. Figure S2 in [56] shows that $\sigma_{xy}/P < \sigma_{\text{ext},xy}P_{\text{ext}}$. Beyond the

applied stress tensor, the barostat also requires two input parameters $P_{\text{damp}} = 0.2256\sqrt{\bar{m}/k_n}$ and $f_{\text{drag}} = 0.05$. The pressure damping P_{damp} adjusts how quickly the box responds to pressure fluctuations in order to maintain the applied stresses. The value $P_{\text{damp}} = 0.2256\sqrt{\bar{m}/k_n}$ is picked so that simulations reach steady state in a relatively short time. Values of $P_{\text{damp}} = 2.256$ and $P_{\text{damp}} = 0.1128$ are also used in simulations of $N = 10^4$ and $P = 10^{-4}$, 10^{-5}, and 10^{-6}. Changing P_{damp} shifts the range of inertial numbers I accessible to these stress-controlled simulations, but does not change the average steady-state behavior of $\mu(I)$ or $\phi(I)$. The effect of P_{damp} on fluctuations is more complicated and is discussed in Sec. III B and shown in Figs. S5 and S6 in [56].

To stabilize these out-of-equilibrium simulations, particularly when in transit to the steady state, the drag factor f_{drag} scales the box change acceleration. The simulation box under steady-state flow continually deforms due to the difference between the external applied stress $\boldsymbol{\sigma}_{\text{ext}}$ and the internal measured stress $\boldsymbol{\sigma}$. The properties presented are calculated using the internal stress.[1]

Simulations are performed using LAMMPS [57,58] to integrate Newton's second law with the velocity-Verlet integration scheme. The simulation time step is set to $\delta t = 0.02\sqrt{k_n/\bar{m}}$. Time steps of $0.01\sqrt{k_n/\bar{m}}$ and $0.005\sqrt{k_n/\bar{m}}$ are also run for a range of applied external shear-stress ratios $\mu_{\text{ext}} = \tau_{\text{ext}}/P_{\text{ext}}$ and P_{ext} for $N = 10^4$. The different time steps do not show a difference in the measured property behavior.

For each applied shear stress, pressure, and system size, three realizations of particles are initialized and simulated. Property uncertainties are calculated from the individual simulations and across the different realizations. Uncertainties are propagated from block averaging of individual runs [59] and as the standard deviation from the three different simulations over the steady-state region in time. Steady-state flow is determined if the measured property uncertainties reach a plateau, with respect to the data blocks used in the block averaging [59]. Simulations are run at steady state at least twice as long as the time required to reach steady state. Total simulation time varies depending on the pressure applied, ranging from 2×10^4 to $1.6\times10^7\sqrt{k_n/\bar{m}}$. The system size, compared to the pressure, has little effect on the transient time. A simulation is not used if any of the three configurations arrests (arrest is identified if the strain rate is below a critical value $\dot{\gamma} > 10^{-9}\sqrt{\bar{m}/k_n}$ [34]) or disobeys simple shear flow.[2] Multiple pressures $P = 10^{-7}$, 10^{-6}, 10^{-5}, 10^{-4}, 10^{-3}, and 10^{-2} and system sizes $N = 3\times10^2$, 10^3, 3×10^3, 10^4, 3×10^4, and 10^5 are simulated (27 total P and N states and 1728 total simulations). A pressure of $P = 10^{-2}$ is above the yield stress of many materials, such as glass, and thus a real material is expected to exhibit different behavior than these nondeformable particles at higher pressures $P > 10^{-3}$.

Flow properties are defined with a tensorial formulation of a general rheological model [6]. Applying the tensorial methodology to the stress-controlled flow data defines the shear-stress ratio and the first and second normal stress difference ratios to pressure. The first-order contribution $\mu = \tau/P$ to the flow is calculated as the rotationally invariant shear stress in the system

$$\mu = \frac{1}{2\dot{\gamma}P}\boldsymbol{\sigma} : \mathbf{D}, \tag{3}$$

[1]The internal stress is calculated from the interparticle forces and kinetic energy $\sigma_{\alpha\beta} = 1/V\sum_i(\sum_{j\neq i} 1/2 r_{\alpha,ij} f_{ij} + m_i v_{\alpha,i} v_{\beta,i})$, where $r_{\alpha,ij}$ and $f_{\alpha,ij}$ are the separation distance and force between particles i and j in the α Cartesian direction, and m_i and $v_{\alpha,i}$ are the ith particle mass and velocity in the α direction, respectively.

[2]Simple shear was quantified as $|\beta| < 0.95$, where β is the vorticity parameter from Giusteri and Seto [60]. Specifically, $\beta = \frac{1}{\dot{\gamma}}\frac{\mathbf{W}:\mathbf{G}}{\mathbf{G}:\mathbf{G}}$, where $\mathbf{G} = \hat{\mathbf{d}}_3\hat{\mathbf{d}}_1 - \hat{\mathbf{d}}_1\hat{\mathbf{d}}_3$, with $\hat{\mathbf{d}}_1$, $\hat{\mathbf{d}}_2$, and $\hat{\mathbf{d}}_3$ are the orthonormal eigenvectors of the symmetric strain rate tensor $\mathbf{D}$ in decreasing order of eigenvalues. Specifically, $\hat{\mathbf{d}}_1$ represents the compression and $\hat{\mathbf{d}}_3$ represents the expansion directions in the plane of the shear flow. The vorticity parameter β is used to quantify the flow behavior, where $\beta = 1$ corresponds to simple shear and $\beta = 0$ corresponds to elongational flow [6].

where $\boldsymbol{\sigma}$ is the Cauchy stress tensor, $\dot{\gamma} = 1/2|\mathbf{D}|$ is the strain rate, measured from the box deformation, $P = 1/3\mathrm{tr}(\boldsymbol{\sigma})$ is the measured pressure, and $\mathbf{D}$ is the strain rate tensor.

Non-Newtonian fluids, including granular flows, typically have second-order contributions to the stress in shear flow which can be characterized by normal stress differences [61]. In the general rheological model from Srivastava *et al.* [6] the second normal stress difference

$$\frac{N_0}{P} = -\frac{3}{2\dot{\gamma}^2 P}\boldsymbol{\sigma} : \left(\mathbf{D}^2 - \frac{\mathrm{tr}(\mathbf{D}^2)}{3}\mathbf{I}\right) \tag{4}$$

is the difference between the mean normal stress in the flow plane and normal stress in the vorticity direction. The second-order contributions to the flow representing the difference between the two normal stresses in the flow plane

$$\frac{N_1}{P} = \frac{1}{2\dot{\gamma}^2 P}\boldsymbol{\sigma} : (\mathbf{DW} - \mathbf{WD}) \tag{5}$$

is the first normal stress difference where the vorticity tensor $\mathbf{W} = \frac{1}{2}(\boldsymbol{\nabla}\mathbf{v} - \boldsymbol{\nabla}\mathbf{v}^{\mathrm{T}})$. For homogeneous simple shear-stress flow, the second and first normal stress differences can equivalently be defined as $N_0/P = (2\sigma_{zz} - \sigma_{yy} - \sigma_{xx})/2P$ and $N_1/P = (\sigma_{yy} - \sigma_{xx})/P$, respectively [13].

III. RESULTS

A. Rheology

Experimental, industrial, and natural granular material have a range of system sizes. A benefit of granular system modeling is that it is tractable and practical to simulate real processes where different boundaries impact rheology, such as rotating drums and split-bottom Couette cells with spherical discrete-element particles. System size plays a role in different geometries [30,62] and therefore it is important to understand system size N and pressure P effects in bulklike rheology which exists in most flows. Bulklike simple shear flow with periodic boundaries in discrete element method simulations are presented in this section.

Figure 1 illustrates the time progression of microstructural and flow properties. The inertial number I, shear-stress ratio μ, volume fraction ϕ, and coordination number Z are plotted against time. Each property is shown for two different pressures $P = 10^{-4}$ (left panels) and $P = 10^{-6}$ (right panels) and for different system sizes, shown as different colors. Neither pressure nor system size impact the steady-state average μ and ϕ at the same I for the two pressures. However, P and N impact the average coordination number Z and fluctuations of all properties. Fluctuations and Z are analyzed and discussed in Sec. III B.

Early times in Fig. 1 show the transition from a very dilute ($\phi = 0.05$) gaslike starting state to a flowing dense, quasistatic regime. Decreasing the pressure increases the time to reach steady state due to the pressure control protocol [52] ($t_{\text{steady state}} \propto P^{-1/2}$). The transient process to steady state is studied elsewhere [34] and is not the subject of this study.

As discussed in Sec. II, an external pressure and shear stress are applied in these simulations. The external pressure and shear-stress ratio are simulation inputs and not necessarily equal to the steady state measured P and μ. Figure 1 shows that $\mu < \mu_{\text{ext}}$ and that as P decreases, more μ_{ext} is required to reach the same I [see Fig. S2 in [56] for more data on $\mu(\mu_{\text{ext}})$]. The simulation box and volume fraction fluctuate around the steady-state value, unlike volume-controlled simulations.

Within the steady flow regime, all the systems studied here, i.e., spanning system sizes and applied pressures, exhibit the expected $\mu(I)$ rheology, as shown in Fig. 2. More specifically, Figs. 2(a) and 2(b) show that for lower pressures ($P < 10^{-3}$), $\mu(I)$ and $\phi(I)$ give very similar results, regardless of pressure or system size, whereas higher pressures $P \geqslant 10^{-3}$ have a noticeable shift

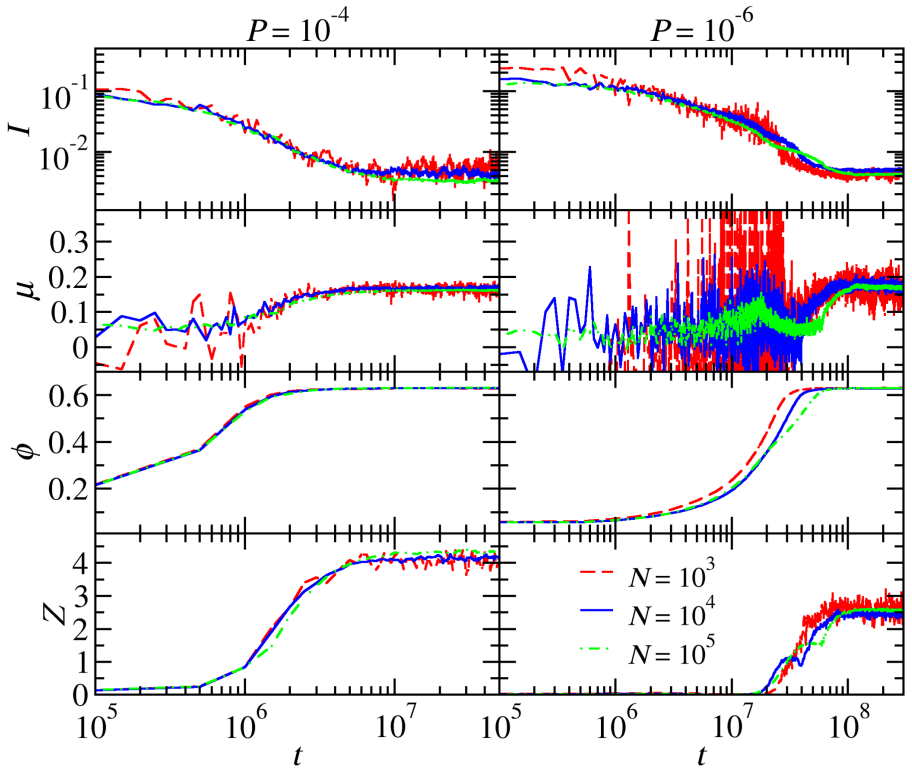

FIG. 1. Inertial number I, measured stress ratio μ, volume fraction ϕ, and coordination number Z, as a function of time t, for three system sizes N. Two pressures are shown: $P = 10^{-4}$ (left-hand panels) and $P = 10^{-6}$ (right-hand panels). Different applied shear-stress ratios are shown for each P and N, at similar $I \simeq 5\times10^{-3}$: $\mu_{\rm ext} = 0.2, 0.193, 0.18$ for $P = 10^{-4}$ and $\mu_{\rm ext} = 0.4, 0.445, 0.4$ for $P = 10^{-6}$ for $N = 10^3$, 10^4, 10^5, respectively.

in value and correspond to particle stiffness values sufficient to model interparticles linear elastic contact behavior discussed in the methodology. A power law, of the form

$$\mu(I) = \mu_c + A_\mu I^{\alpha_\mu}, \tag{6}$$

$$\phi(I) = \phi_c - A_\phi I^{\alpha_\phi}, \tag{7}$$

is fit to the rheology data and is drawn as the lines in Fig. 2. From the power-law fits, critical values μ_c and ϕ_c are extracted individually for each of the system sizes and pressures as the value corresponding to the limits $\mu_c \equiv \lim_{I\to 0}\mu$ and $\phi_c \equiv \lim_{I\to 0}\phi$, respectively. The shifted data $\mu - \mu_c(P,N)$ and $\phi - \phi_c(P,N)$ are shown in Figs. 2(c) and 2(d) and demonstrate that all the data are fit well by Eqs. (6) and (7). The shifted μ and ϕ data also demonstrate that the critical low-strain values μ_c and ϕ_c account for the impact of higher pressures $P \geqslant 10^{-3}$. The decrease of $\phi - \phi_c(P,N)$ away from the fitting line shows that fitting leads to a systematic small, order 10^{-3}, overestimation of $\phi_c(P,N)$. The fit values are plotted in Fig. 3.

As visually apparent from Fig. 2, most of the fit values in Fig. 3 are system-size independent with some important exceptions. Higher-pressure $P \geqslant 10^{-3}$ fit values do show a statistically significant dependence on N in μ_c, α_μ, and ϕ_c, as observed by Peyneau and Roux for μ_c and ϕ_c [31]. The other fit parameters A_μ, A_ϕ, and α_ϕ depend on P but not N. The exponents α_μ and α_ϕ are not constant with N and P when allowed to vary. Good quality fits ($R^2 > 0.986$) and discernible change in the

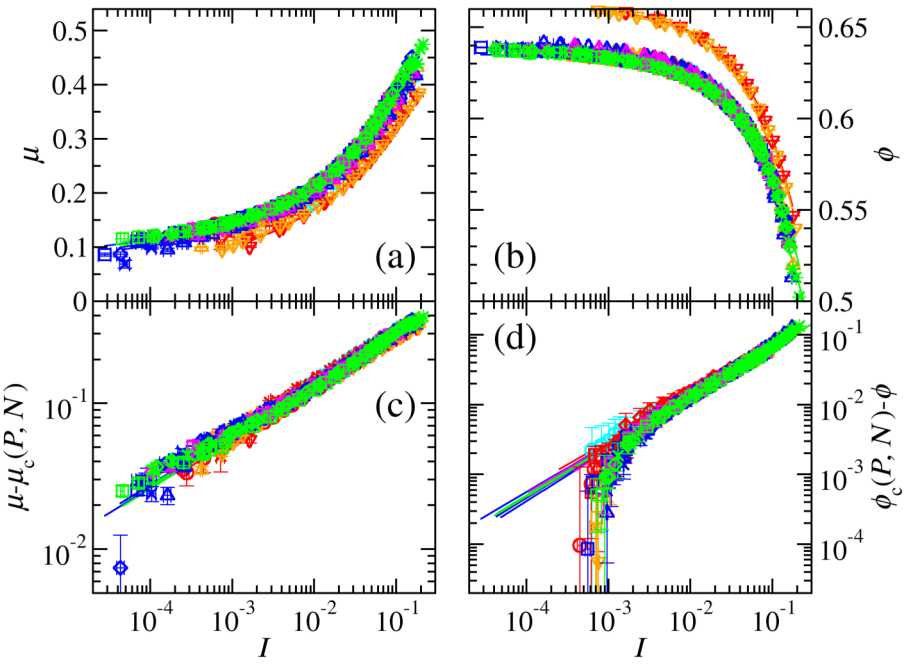

FIG. 2. (a) Stress ratio $\mu = \tau/P$ and (b) volume fraction ϕ as a function of the inertial number. The distances from the zero-inertial number limit, (c) $\mu - \mu_c(P, N)$ and (d) $\phi - \phi_c(P, N)$, illustrate the sensitivity of the power-law exponent. Each symbol represents simulation data averaged over three runs at different applied stress, pressure (symbol shape), and system size (symbol color). Simulations were run with $N = 3\times10^2$ (cyan), 10^3 (red), 3×10^3 (orange), 10^4 (blue), 3×10^4 (magenta), and 10^5 (green) for $P = 10^{-7}$ (circles), 10^{-6} (squares), 10^{-5} (diamonds), 10^{-4} (crosses), 10^{-3} (up triangles), and 10^{-2} (down triangles).

other fit value trends can be attained by setting $\alpha_\mu(P, N) = 0.35$, as proposed by DeGiuli *et al.* [47]. However, better fits are attained when $\alpha_\mu(P, N)$ is allowed to vary, as shown in Fig. 3. In Fig. S3 in [56], the same data as in Fig. 3 are shown with P on the x axis, to aid in understanding the impact of N and P.

Making comparisons with experimental systems benefit from identifying the limit of infinitely large $N \to \infty$ and rigid particle $P \to 0$ systems. The N and P dependence of the $\mu(I)$ and $\phi(I)$ fit parameters are quantified in Table SI of Supplemental Material [56]. For the volume fraction fitting parameters, $\phi_{c,N\to\infty,P\to0} = 0.633 \pm 0.001$, $A_{\phi,N\to\infty,P\to0} = -0.34 \pm 0.02$, and $\alpha_{\phi,N\to\infty,P\to0} = 0.71 \pm 0.04$. For the stress ratio fitting parameter fits, $\mu_{c,N\to\infty,P\to0} = 0.13 \pm 0.02$, $A_{\mu,N\to\infty,P\to0} = 0.84 \pm 0.01$, and $\alpha_{\mu,N\to\infty,P\to0} = 0.50 \pm 0.03$. Table SI in the Supplemental Material [56] reports full information on the fits to $\phi_c(N, P)$, $A_\phi(N, P)$, $\alpha_\phi(N, P)$, $\mu_c(N, P)$, $A_\mu(N, P)$, and $\alpha_\mu(N, P)$. Kawasaki *et al.* [32] found similar values for frictionless three-dimensional spheres. Differences between the results of Table SI and Kawasaki *et al.* [32] may be due to the fitting procedure differences or smaller system sizes ($10^2 < N < 10^4$).

The fit values in Fig. 3 can be sensitive to the range of inertial numbers. Only inertial numbers I that are available to all P and N runs ($6\times10^{-3} < I < 6\times10^{-2}$) are used in the fitting procedure so that comparisons throughout the range including all simulations is four orders of magnitude ($3\times10^{-5} < I < 2\times10^{-1}$). Therefore, a wide range of inertial numbers are collected to ensure the fits are representative of the quasistatic and inertial flow regimes. Collecting data for low inertial numbers requires longer simulations because of the larger fluctuations and longer transient times, up to approximately two times longer. In these stress-controlled simulations the inertial number is limited on the low end by the transition to stick-slip and arrest behavior. For higher inertial numbers

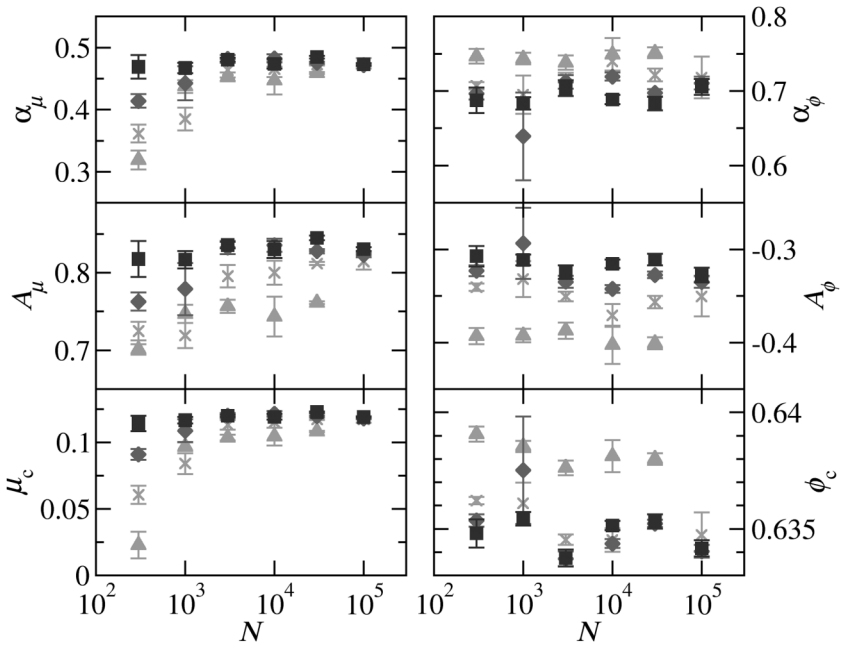

FIG. 3. Power-law fit parameters to the stress ratio $\mu(I)$ (three left panels) and volume fraction $\phi(I)$ (three right panels) using Eqs. (6) and (7), respectively. The exponents α_μ and α_ϕ, prefactors A_μ and A_ϕ, and critical values μ_c and ϕ_c are shown as a function of the number of particles N. Different applied pressures are shown as different symbols: $P = 10^{-6}$ (squares), $P = 10^{-5}$ (diamonds), $P = 10^{-4}$ (crosses), and $P = 10^{-3}$ (triangles).

the system dilutes and fewer contacts contribute to the internal stress. Larger strain rates and inertial numbers are thus not accessible to stress-controlled simulations because the flow is driven by the difference in external and internal stress.

Although the arresting flows observed in stress-controlled simulations limit the fitting range of I, the method gives an estimate of the flow-to-arrest transition system-size dependence. Figure 4 shows the maximum applied stress where a flow-to-arrest transition is observed $\mu_{c,\text{arrest}}$ as a function of the number of particles for two pressures. The critical stress ratios extracted from the power-law fit to the data $\mu_{c,\text{fit}}$ are another measure of arrest. For large systems, $\mu_{c,\text{arrest}}$ and $\mu_{c,\text{fit}}$ agree. As the system size decreases, the values of μ_c for different methods diverge; specifically, $\mu_{c,\text{arrest}}$ increases and $\mu_{c,\text{fit}}$ decreases.

Arrest is naturally observed in these bulklike stress-controlled simulations with periodic boundaries. As the system size decreases, so does the length of a force chain needed to span the simulation box, and the transition from flow to arrest occurs more frequently and at higher inertial numbers. The system-size dependence of $\mu_{c,\text{arrest}}$ affects the accessible strain rates and I. At low system sizes, there is a smaller range of I to fit, which typically leads to a lower $\mu_{c,\text{fit}}$.

Figure 4 also shows that $\mu_{c,\text{arrest}}$ is not pressure dependent, unlike $\mu_{c,\text{fit}}$. The disagreement between $\mu_{c,\text{arrest}}$ and $\mu_{c,\text{fit}}$ for low N illustrates the importance of system size for characterizing and fitting the $\mu(I)$ rheology in the quasistatic limit. The fit to data with $N = 3\times10^2$ and $P = 10^{-3}$, for example, predicts that applying a stress ratio greater than 0.03 is sufficient to keep the granular material flowing; however, the small systems arrest quickly at a stress ratio that low. The $\mu_{c,\text{arrest}}(N) \simeq N^{-1/2}$ dependence has been observed previously by Peyneau and Roux [31] and is plotted as the line in Fig. 4. Peyneau and Roux [31] used static stress-controlled simulations, starting from zero-shear stress and incrementally increasing the stress until steady-state flow was observed. The hysteresis of flow to arrest and arrest to flow could explain why $\mu_{c,\text{arrest-to-flow}}(N) > \mu_{c,\text{flow-to-arrest}}(N)$.

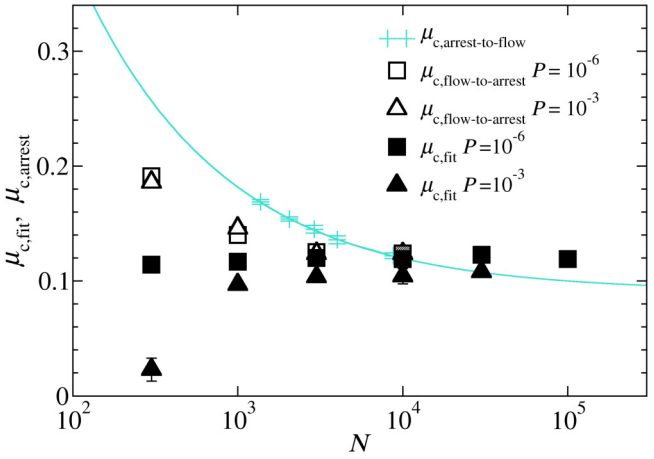

FIG. 4. Critical stress ratio calculated by fitting Eq. (6) to $\mu(I)$, $\mu_{c,\text{fit}}$, and calculated as the maximum applied stress where arrest was observed $\mu_{c,\text{arrest}}$. Arrest was not observed for $N > 3\times10^3$ and therefore $\mu_{c,\text{arrest}}$ for $N > 3\times10^3$ are not presented. The shaded point at $N = 10^4$ is from Srivastava *et al.* [34], which is a rigorous estimate of the value. Cyan symbols are from static stress-controlled simulations going from arrest to flow and the cyan line is a fit $0.091 + 2.87N^{-1/2}$ [31].

Hysteresis of the critical stress to flow has been observed in other flow geometries, such as the difference between θ_{start} and θ_{repose} for flow down an incline [48,63]. All the simulated $\mu_{c,\text{arrest}}$ data presented here represent the flow-to-arrest transition $\mu_{c,\text{flow-to-arrest}}$, except for that from Peyneau and Roux [31], which is $\mu_{c,\text{arrest-to-flow}}$.

Like the critical stress required to flow granular material, the nonzero first and second normal stress differences distinguish granular flows from simple Newtonian fluids [6,35]. The first N_1/P and second N_0/P stress differences are shown in Figs. 5(b) and 5(a), respectively. The second normal stress difference is negative in all flows and approaches a nonzero plateau, as the inset of Fig. 5(a) highlights. The negative values of N_0/P are due to larger normal stress, and the number of contacts, in the flow plane as compared to the neutral, vorticity direction, and that difference, decreases as $I \to 0$. These results are counter to some rheologies that expect $N_0 \to 0$ as $I \to 0$ for frictionless granular flows [6]. As shown in Fig. 5(b), N_1/P changes from positive to negative as the flow slows. This behavior has been observed previously in experiments [64] and simulations [6,10,12,13], but is debated.

Both N_0/P and N_1/P have stronger pressure dependence than μ and ϕ, and large system sizes demonstrate important features. The inset of Fig. 5(b) shows that in the dense-flow regime N_1/P has a minimum. The minimum is most convincing and statistically certain for the larger system sizes $N \geqslant 10^4$, which demonstrates the importance of large system sizes for measuring higher-order flow properties. The minimum has also been observed in other flow conditions, including flow down an incline in two dimensions [48]. One explanation in these simple shear simulations is the misalignment between the fabric and strain-rate tensors [6,13]. The power-law fit used for $\mu(I)$ does not describe $N_1/P(I)$ at low inertial numbers because of the minimum.

Seto and Giusteri observed that dense suspensions also have nonzero plateaus in N_1/P and that the plateau goes to zero as the particle spring constant increases (a 100× increase in spring constant led to a 10× decrease in the N_1/P plateau) [13]. In the presented data, there is no pressure dependence in the low-I regime across five orders of magnitude of P. The N_0/P and N_1/P for other time steps are shown in Fig. S4 in [56]. Because decreasing the time step does not impact the mean values of either N_0/P or N_1/P, it is ensured that the time step $\delta t = 0.02\sqrt{k_n/\bar{m}}$ is not too large to capture the small fluctuations in stress at low inertial numbers (a concern posed by Seto and Giusteri [13]), at least for these stress-controlled simulations of dry frictionless particles.

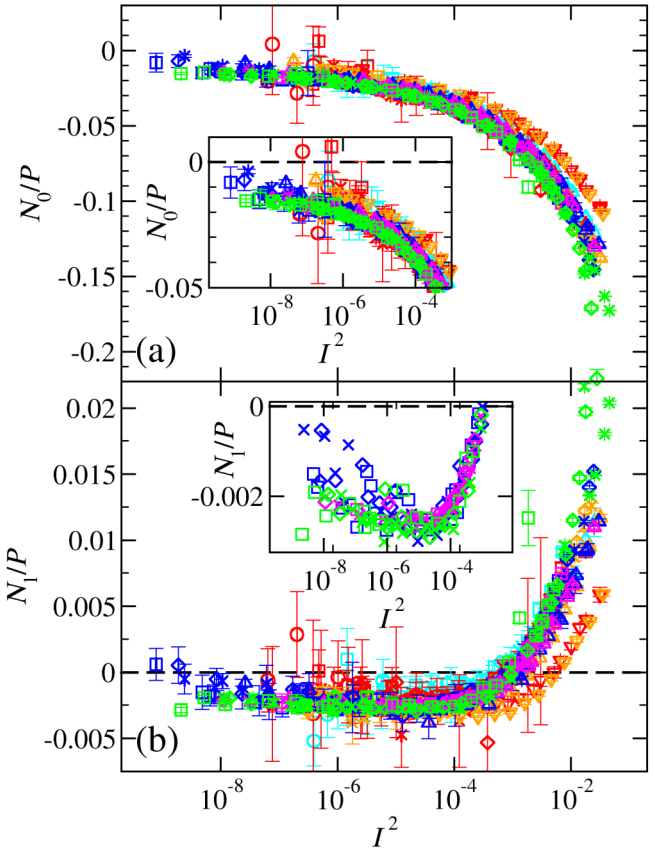

FIG. 5. (a) Second N_0/P and (b) first N_1/P normal stress difference ratios normalized by pressure [see Eqs. (4) and (5)] as a function of I^2. System sizes and pressures are the same as in Fig. 2. The inset of (b) shows a close-up near the quasistatic limit of the three larger system sizes ($N = 10^4$, 3×10^4, and 10^5).

B. Fluctuations

The transition from quasistatic to inertial granular flow is gradual in the average values of $\mu(I)$, $\phi(I)$, $N_1(I)$, and $N_0(I)$. Fluctuations about those averages, however, have been very useful for signaling transitions. For example, in the approach to jamming, velocity [65] and viscosity [66] fluctuations become discontinuous. Velocity fluctuations can also signal the transition from critical and plastic regimes in granular flows [27]. Fluctuations can characterize nonlocal effects [7] and comparisons between geometries [26]. In particular, particle stiffness, or pressure, impacts strain rate and kinetic energy fluctuations in granular flow and leads to different flow regimes [33]. In the preceding section the range of accessible I values was limited in low system sizes, because of the large fluctuations that lead to arrest. It is therefore important to study the impact of system size N and pressure P on fluctuations.

The time series shown in Fig. 1 illustrates the fluctuation of kinematic (I), mechanical (μ), and microstructural (ϕ and Z) properties and how they depend on P and N about their mean. The variance of those properties over the steady flow period quantifies those fluctuations. The variance of the shear stress τ is defined as $\Delta\tau \equiv \frac{1}{N_{\rm samp}}\sum_{i=1}^{N_{\rm samp}}[\tau(t)-\bar{\tau}]^2$ over the steady-state simulation data. In addition to $\dot{\gamma}$, τ, ϕ, and Z, we also analyze fluctuations in the stress differences N_0 and N_1 and structural anisotropy of the particle contact network. The structural anisotropy of the contact network is quantified by the second invariant of the deviatoric contact anisotropy tensor a_c. The

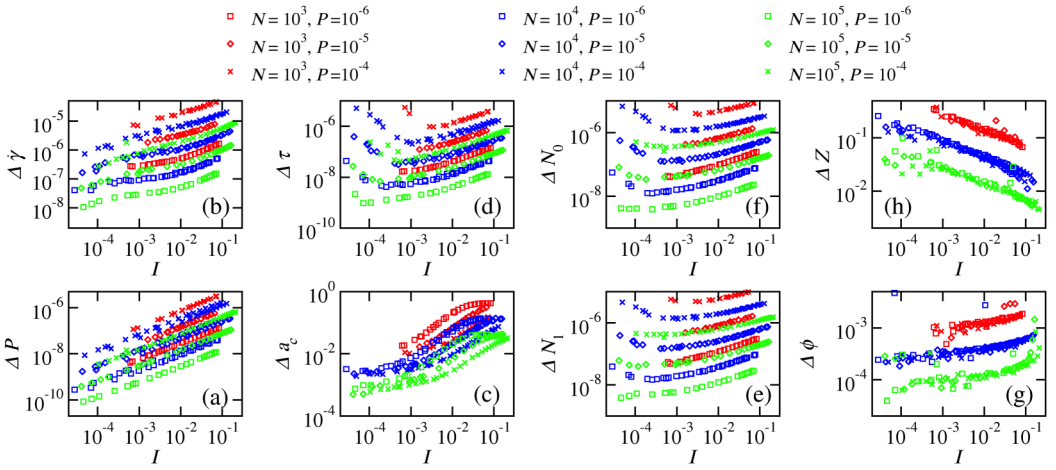

FIG. 6. Variance of steady-state fluctuations of the following parameters as a function of the measured steady-state inertial number I: (a) pressure P, (b) strain rate $\dot{\gamma}$, (c) contact fabric anisotropy a_c, (d) shear stress τ, (e) first normal stress difference N_1, (f) second normal stress difference N_0, (g) volume fraction ϕ, and (h) coordination number Z. The colors and symbols represent different N and P and are the same as in Fig. 2.

tensor components of a_c in the i and j directions are $a_{c,ij} = \frac{15}{2}R'_{ij}$ and the contact fabric tensor, based on the contact normals n_i of N_c total contacts, is $R'_{ij} = \frac{1}{N_c}\sum_{N_c} n_i n_j$ [67]. The variance of flow properties is shown as a function of inertial number in Fig. 6.

The variance of most properties increases with increasing inertial number, including ΔP, $\Delta\dot{\gamma}$, Δa_c, and $\Delta\phi$, whereas for ΔZ, as the system flows faster, the fluctuations decrease. The flow properties $\Delta\tau$, ΔN_1, and ΔN_0 have a nonmonotonic dependence on I; $\Delta\tau$, ΔN_1, and ΔN_0 behave like the other properties, above a critical $I > I_c$. Below that critical $I < I_c$, the fluctuations increase, approaching arrest. As for $\Delta\tau$, ΔN_1, and ΔN_0, velocity fluctuations of flowing granular materials also grow near jamming [65].

Fluctuations of flow properties depend on N and P, beyond the I, unlike the average flow properties. The N and P dependencies of the variance are shown in Fig. 7. Collapse of all the variance data as a function of strain rate $\dot{\gamma}$ and pressure P is possible with different scalings, as shown in the y-axis label in Fig. 7. The fluctuations of each property are scaled as

$$N^a P^b \Delta = P^c I = B\dot{\gamma} P^{-0.5} P^c, \tag{8}$$

where $B = \frac{\bar{d}}{2}\sqrt{\rho_p}$. The exponents a and b are applied to the variance and depend on the property. The properties $\Delta\tau(I)$, $\Delta a_c(I)$, $\Delta N_1(I)$, and $\Delta N_0(I)$ have P-dependent transitions where the slope changes, and thus I is scaled by P^c.

Power-law fits to the scaled variances are shown in Fig. 7. Applying a power-law fit to Eq. (8) leads to

$$N^a P^b \Delta \sim (P^c I)^d, \tag{9}$$

where d is the power-law exponent. Solving Eq. (9) for the variance leads to the scaling law for kinematic, stress, and microstructural property variance

$$\Delta \sim N^{-a}\dot{\gamma}^d P^{d(c-1/2)-b}, \tag{10}$$

where the pressure exponent $e \equiv d(c-1/2) - b$. The exponents of the fits d and the pressure exponent e are shown in Table I.

For all properties, smaller system sizes have larger fluctuations ($a > 0$). An exponent of $a = 1/2$ is expected from the central limit theorem and has been seen previously for $\Delta\phi$ and $\Delta\tau/P$

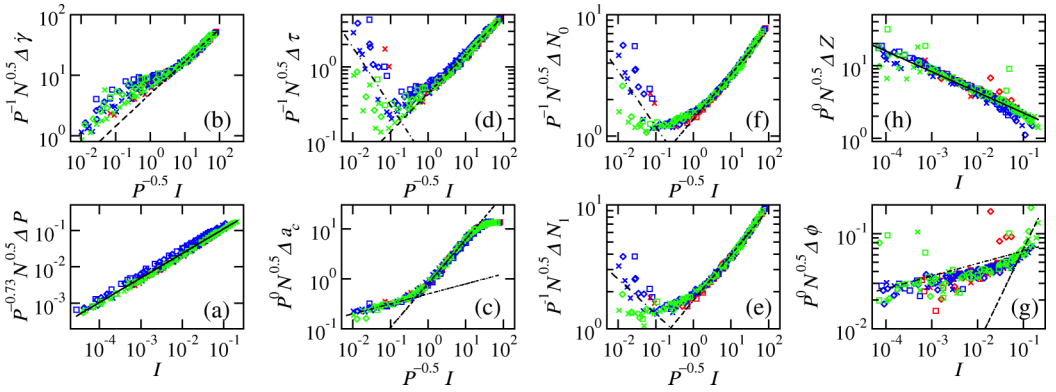

FIG. 7. Variance normalized by N^a and P^b for various properties, which leads to a collapse as a function of the inertial number I, except for the stress values, τ, N_1, N_0, and the fabric anisotropy a_c for which I is normalized by P^c. The normalized variance is fit to a power law over the whole range (solid lines), or a low range (dot-dashed lines) and high range (dashed lines) of I or $P^{-0.5}I$. The exponents of the power-law fits drawn as lines are given in Table I.

of frictionless granular flows [31]. For most of the properties, fluctuations decrease with pressure ($b < 0$). However, the microstructural properties Δa_c, $\Delta\phi$, and ΔZ are P independent ($b = 0$) with respect to the inertial number. The magnitude of the fit exponents $|d|$ varies from 0.12 to 0.880 depending on the specific property.

Although it is expected that at a given inertial number the fluctuations decrease when either P increases or N decreases, the transitions of two different slopes in $\Delta\tau$, Δa_c, ΔN_1, ΔN_0, and $\Delta\phi$ are surprising. The transitions in the normalized fluctuations of τ, N_1, N_0, and a_c, measured for $P^{-0.5}I$ at the intersection of two fits, are statistically consistent, $P^{-0.5}I = 0.2 \pm 0.1$, 0.3 ± 0.1, 0.2 ± 0.1, and 0.5 ± 0.2, respectively. No such transition is observed in the average steady-state values of τ, N_1, N_0, or a_c, which are essentially N and P independent and have the same I dependence, as seen in Figs. 2 and 5.

Thomas *et al.* [20] saw a transition in the slope of the force network fluctuation rate at a similar inertial number $I \simeq 0.06$ in granular flow-down-an-incline experiments. This change in scaling at low $P^{-0.5}I$, which occurs for all the mechanical property fluctuations, could be a quantitative

TABLE I. Exponent values used to scale, normalize (a, b, and c), and fit (d, e, d^+, and e^+) the variance of various properties run for different numbers of particles N and applied pressure as a function of inertial number.

Property	a	b	c	d	e[a]	d^+[b]	e^+[b]
P	0.5	−0.73	0	0.686 ± 0.003	0.387		
$\dot{\gamma}$	0.5	−1	−0.5	0.54 ± 0.01	0.73		
a_c	0.5	0	−0.5	0.20 ± 0.02	−0.1	0.880 ± 0.008	−0.88
τ	0.5	−1	−0.5	-0.8 ± 0.2	1.8	0.519 ± 0.005	0.481
N_1	0.5	−1	−0.5	-0.28 ± 0.08	1.28	0.367 ± 0.003	0.633
N_0	0.5	−0.5	−0.5	-0.5 ± 0.1	1.5	0.369 ± 0.003	0.61
ϕ	0.5	0	0	0.12 ± 0.02	−0.06	0.58 ± 0.07	−0.29
Z	0.5	0	0	-0.28 ± 0.01	0.14		

[a]The variance-pressure exponent $e = d(c - 1/2) - b$.
[b]Property variance with different fits at high strain rates.

measure of the transition from quasistatic to inertial flows. The transitions in the scaling $\Delta\tau$ and Δa_c are similar, because the contact fabric is the primary support for the shear stress [68].

Previous simulations of dry granular flow have also observed large fluctuations in stress [65] and coordination number [51,69] in the approach to jamming. Jammed dry granular material can resemble glasses. Large stress fluctuations in sheared glasses are associated with a transition from a nonmonotonic to a monotonic rheology [70]. Strained binary Lennard-Jones glasses have scaling transitions in stress and kinetic energy fluctuations, observed by Clemmer *et al.* [71]. The stress fluctuations in the glass system scale with $N^{0.5}$, as they do in the flowing dry granular systems presented here. For the glasses, the transition is due to avalanche shear events becoming temporally distinct at slow rates.

The transition in scaling of the normalized $\Delta\tau$ and Δa_c at $P^{0.5}I = 0.2 \pm 0.1$ depends not only on pressure but pressure damping $P_{\rm damp}$. Pressure damping also impacts the fluctuations of ΔP and $\Delta\dot{\gamma}$, properties which are sensitive to the numerical pressure control parameters in the stress-controlled simulation method. See Figs. S5 and S6 in [56] for the impact of $P_{\rm damp}$ on fluctuations in systems with $N = 10^4$ particles with $P = 10^{-4}$, 10^{-5}, and 10^{-6} and $P_{\rm damp} = 2.256$, 0.2256, and 0.1128. Although the average flow properties do not depend on the protocol, Figs. S5 and S6 in [56] show that many property fluctuations do.

Supplemental Material [56] also includes the relative variance in Figs. S7 and S8 and Table SII, normalized by the absolute mean $\bar{\Delta}\tau \equiv \frac{1}{|\bar{\tau}|N_{\rm samp}} \sum_{i=1}^{N_{\rm samp}} [\tau(t) - \bar{\tau}]^2$. Normalizing the variance by the mean value changes the scaling of these fluctuations. A plateau for low pressure in $\bar{\Delta}N_0$ occurs at the transition previously identified. This plateau goes away as the pressure increases. The pressure dependence in $Z(I)$ causes a $\bar{\Delta}Z(I)$ pressure dependence, as is expected. However, the slope of $\bar{\Delta}Z(I)$ changes sign twice as I increases. The quasistatic transition is present for $\bar{\Delta}a_c$, although it is less pronounced.

A $\sqrt{N}$ dependence in $\Delta\tau$, ΔN_1, and ΔN_0 for flows slower than the transition in $P^{-0.5}I$ is shown in Fig. 7. This indicates an additional sensitivity to system size near arrest in the quasistatic regime for τ, N_1, and N_0. The fluctuation scaling in Fig. S8 in [56] shows collapse of $\bar{\Delta}\tau$ when $P^{-0.5}I$ is scaled by the $\sqrt{N}$ dependence in $\bar{\Delta}\tau$ for flows slower than the transition. The additional system-size dependence in the fluctuations ΔN_1 may influence the average first normal stress difference N_1/P, in Fig. 5(b). The spread of $N_1/P(I^2)$ values below the minimum $I^2 < 10^{-4}$ increases as the system size decreases.

Most of the properties presented have P- and N-dependent variances and P- and N-independent averages, and yet the coordination number exhibits the opposite behavior; the variance $\Delta Z(I)$ is pressure independent and the average $Z(I)$ is pressure dependent, as shown in Fig. 8(a). As pressure increases Z shifts to higher I, even though the volume fraction ϕ is pressure independent. Therefore, the inertial number is insufficient to capture the coordination number behavior. The average Z has the same P dependence as the normalized $\Delta\tau$. The collapse in Fig. 8(b) when plotted as a function of $P^{-0.5}I$ demonstrates the added P dependence. Figure 8(b) shows the distance of $Z(I)$ from the pressure- and system-size-dependent jamming coordination number $Z_J(P, N)$, where $Z_J(P, N)$ is calculated using an isotropic pressure-controlled zero-shear protocol [52]. The average packing coordination number scales as $Z_J \sim P^{-0.5}$, as seen previously [72].

In quasistatic flows, $Z(I, P) - Z_J(P, N) \equiv \hat{Z}(I, P)$ depends only on $P^{-0.5}I$. Faster flows ($P^{-0.5}I > 0.2$) depend on pressure. The coordination number $Z(I, P)$ increases with pressure, but $\hat{Z}(I, P)$ decreases at a faster rate as $P^{-0.5}I$ increases for higher pressures. The inertial flow behavior of $\hat{Z}(I, P)$ does not collapse. Chialvo *et al.* [50] observed a similar pressure effect on the shear-stress ratio in volume-controlled simulations of inertial flows that was attributed to the softness of high-pressure systems. A similar approach is used here, by fitting a power law

$$Z(I, P) - Z_J(P, N) \equiv \hat{Z}(I, P) = A_{\hat{Z}}(P^{-0.5}I)^{\alpha_{\hat{Z}}} \tag{11}$$

to the pressure-shifted coordination number distance from jamming. The fitting parameters $A_{\hat{Z}}$ and $\alpha_{\hat{Z}}$ are shown in Fig. S9 in [56]. Both fitting parameters are relatively insensitive to the system size

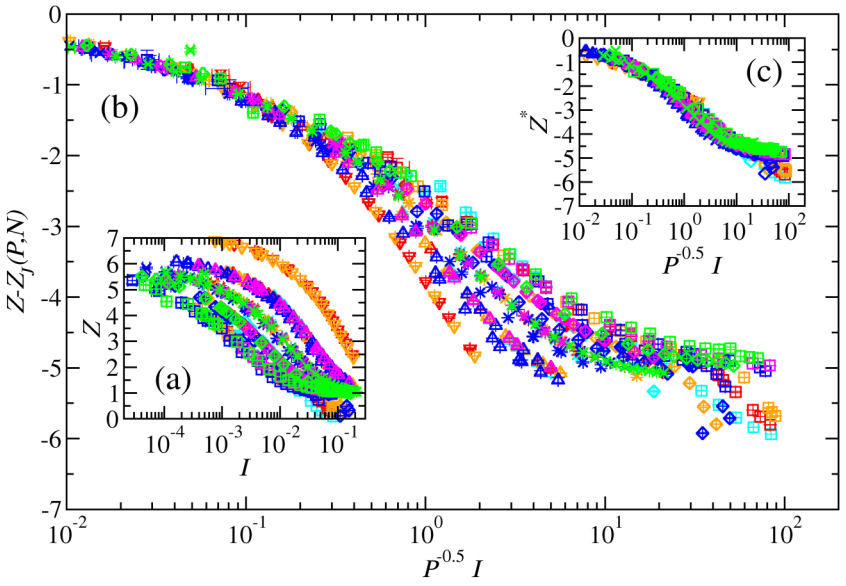

FIG. 8. (a) Coordination number Z as a function of the inertial number I. (b) Distance from the isotropic compression jamming coordination number $Z(I,P) - Z_J(P,N)$ as a function of the pressure-scaled inertial number $P^{-0.5}I$. (c) Hard-sphere limit coordination number $Z^* = Z(I,P) - Z_J(P,N) - \hat{Z}_{\rm soft}(P) + \hat{Z}_{\rm hard}$ as a function of the pressure-scaled inertial number $P^{-0.5}I$. Colors and symbols are the same as in Fig. 2.

N; however, they both have a pressure dependence. The power-law fitting parameters are well fit to the square of the pressure $\alpha_{\hat{Z}} = \alpha_{\hat{Z},c} + B_{\alpha_{\hat{Z}}}\sqrt{P}$ and $A_{\hat{Z}} = A_{\hat{Z},c} + B_{A_{\hat{Z}}}\sqrt{P}$. The hard-sphere behavior $P \to 0$ is extrapolated from the fitting parameters to be

$$\hat{Z}_{\rm hard}(P^{-0.5}I) = -2.592(P^{-0.5}I)^{0.2861} \tag{12}$$

(see the Supplemental Material [56] for more information). Figure 8(c) shows the distance of the pressure-dependent soft-sphere behavior from the hard-sphere behavior. When the soft-to-hard distance is subtracted from the simulated data

$$Z^* = \hat{Z}(I,P) - \hat{Z}_{\rm soft}(I,P) + \hat{Z}_{\rm hard}(P^{-0.5}I) \tag{13}$$

there is collapse across P.

IV. CONCLUSION

Power-law scalings of the fluctuations in various kinematic, mechanical, and microstructural properties with pressure and system size were quantified in dense flows of dry frictionless granular materials. Between 3×10^2 and 10^5 three-dimensional spherical particles flowed under simple shear in stress-controlled discrete-element particle-based simulations. Power-law relationships between the mean steady-state values of the stress ratio μ, volume fraction ϕ, and second normal stress N_0/P as a function of the inertial number I were demonstrated. Unlike those properties, the first normal stress N_1/P shows a nonmonotonic variation with I which cannot be captured by the typical power-law fits and requires large system sizes to measure with certainty. Power-law fits are consistent across N and P, for large systems sizes $N \geqslant 1000$ and low pressures $P < 10^{-3}$. A wide range of I is needed to attain reliable fits that are comparable across N and P, which requires many simulations.

The lower range of I is limited by arrest near the critical shear stress, especially in the stress-controlled method used, where the arrest occurs stochastically. The arrest stress ratio, along with fitted critical stress ratio, show strong system-size dependence at lower pressures. Furthermore,

the arrest $\mu_{c,\text{arrest}}$ and fitted critical $\mu_{c,\text{fit}}$ stress ratios have opposite dependencies to system size. The N dependence of $\mu_{c,\text{fit}}$ in the stress-controlled simulations are the opposite of what has been seen in strain-controlled simulations, because arresting flows limit the range of I available, giving more freedom for the fitting procedure. A more detailed measurement and characterization of the flow-to-arrest and arrest-to-flow transitions for different system sizes are subjects left for future study.

System size and pressure effects on fluctuations in steady flowing properties are considerably more pronounced than in the averaged properties. The averages of μ, ϕ, N_0/P, and N_1/P have the same relationship to inertial number regardless of N and P. The fluctuations of each property, however, vary differently with P. All fluctuations scale with $\sqrt{N}$, consistent with the central limit theorem. The impact of P on fluctuations differs in that they are either independent of P ($\Delta\phi$ and ΔZ), scale with P (exponent magnitudes less than 1 for $\Delta\phi$, Δa_c, and ΔZ), or scale strongly with P (exponent magnitudes greater than 1 for $\Delta\tau$, ΔN_1, and ΔN_0). Furthermore, P impacted the fluctuation scaling with respect to inertial number for many properties. Specifically, $\Delta\tau$, Δa_c, ΔN_1, and ΔN_0 do not collapse with I, but with $P^{-0.5}I$ and have a pressure-dependent transition at $P^{-0.5}I \simeq 0.2$. At that transition the slopes of $\Delta\tau(I)\Delta N_1(I)$ and $\Delta N_0(I)$ change sign. Power-law fits to those fluctuations above and below the transition were presented. The transition in the variance of shear stress is a potential quantitative measure of the boundary between quasistatic and inertial flow regimes.

Interestingly, fluctuations in the coordination number are not pressure sensitive, while the average coordination number is sensitive to pressure. The opposite behavior was observed in ϕ, μ, N_1, and N_0. The average $Z(I)$ is pressure dependent, unlike the other properties presented, and requires I to be scaled by $P^{-0.5}I$, as was seen in $\Delta\tau$, Δa_c, ΔN_1, and ΔN_0. The pressure dependence in the coordination number flow behavior in the quasistatic flow regime is captured by $Z - Z_J = \hat{Z}(P^{-0.5}I)$. In the inertial regime, there is an additional pressure dependence stemming from effective particle softness in faster flows. We take the limiting behavior of $\hat{Z}(P^{-0.5}I)$ to define the hard-sphere-limit behavior, and the distance from that hard-sphere limit accounts for the additional pressure dependence of the coordination number in the inertial regime. The connection between Z and flow fluctuations in dry granular flow is a promising area for future work.

This comprehensive study quantifies not just the steady-state values of important microstructural metrics such as coordination and fabric anisotropy in dense granular flows, but also the fluctuations of these properties and their system-size scaling. These results could greatly contribute towards the development of microstructure-aware constitutive models for granular flows, particularly those that include the role of fluctuations, as was demonstrated previously for dilute granular gases [73]. Such a model could be very useful for small confined systems where fluctuations have a crucial role. Ongoing work includes the effect of sliding, rolling, and twisting friction on dry granular flow.

ACKNOWLEDGMENTS

I.S. acknowledges support from the U.S. Department of Energy, Office of Science, Office of Advanced Scientific Computing Research, Applied Mathematics Program under Contract No. DE-AC02-05CH11231. This work was supported by the Sandia Laboratory Directed Research and Development Program. This work was performed, in part, at the Center for Integrated Nanotechnologies, an Office of Science User Facility operated for the U.S. Department of Energy (DOE) Office of Science. Sandia National Laboratories is a multimission laboratory managed and operated by National Technology and Engineering Solutions of Sandia, LLC., a wholly owned subsidiary of Honeywell International, Inc., for the U.S. DOE's National Nuclear Security Administration under Contract No. DE-NA-0003525. The views expressed in the article do not necessarily represent the views of the U.S. DOE or the United States Government.

[1] G. D. R. Midi, On dense granular flows, Eur. Phys. J. E **14**, 341 (2004).
[2] P. Jop, Y. Forterre, and O. Pouliquen, A constitutive law for dense granular flows, Nature (London) **441**, 727 (2006).
[3] M. Renouf, D. Bonamy, F. Dubois, and P. Alart, Numerical simulation of two-dimensional steady granular flows in rotating drum: On surface flow rheology, Phys. Fluids **17**, 103303 (2005).
[4] N. Huang, G. Ovarlez, F. Bertrand, S. Rodts, P. Coussot, and D. Bonn, Flow of Wet Granular Materials, Phys. Rev. Lett. **94**, 028301 (2005).
[5] P. Jop, Y. Forterre, and O. Pouliquen, Crucial role of sidewalls in granular surface flows: Consequences for the rheology, J. Fluid Mech. **541**, 167 (2005).
[6] I. Srivastava, L. E. Silbert, G. S. Grest, and J. B. Lechman, Viscometric flow of dense granular materials under controlled pressure and shear stress, J. Fluid Mech. **907**, A18 (2021).
[7] D. L. Henann and K. Kamrin, A predictive, size-dependent continuum model for dense granular flows, Proc. Natl. Acad. Sci. USA **110**, 6730 (2013).
[8] V. Mehandia, K. J. Gutam, and P. R. Nott, Anomalous Stress Profile in a Sheared Granular Column, Phys. Rev. Lett. **109**, 128002 (2012).
[9] F. Boyer, O. Pouliquen, and É. Guazzelli, Dense suspensions in rotating-rod flows: Normal stresses and particle migration, J. Fluid Mech. **686**, 5 (2011).
[10] M. Alam and S. Luding, First normal stress difference and crystallization in a dense sheared granular fluid, Phys. Fluids **15**, 2298 (2003).
[11] M. Depken, J. B. Lechman, M. van Hecke, W. van Saarloos, and G. S. Grest, Stresses in smooth flows of dense granular media, Europhys. Lett. **78**, 58001 (2007).
[12] T. Weinhart, R. Hartkamp, A. R. Thornton, and S. Luding, Coarse-grained local and objective continuum description of three-dimensional granular flows down an inclined surface, Phys. Fluids **25**, 070605 (2013).
[13] R. Seto and G. G. Giusteri, Normal stress differences in dense suspensions, J. Fluid Mech. **857**, 200 (2018).
[14] J. T. Clemmer, I. Srivastava, G. S. Grest, and J. B. Lechman, Shear Is Not Always Simple: Rate-Dependent Effects of Flow Type on Granular Rheology, Phys. Rev. Lett. **127**, 268003 (2021).
[15] D. C. Drucker and W. Prager, Soil mechanics and plastic analysis or limit design, Q. Appl. Math. **10**, 157 (1952).
[16] O. Pouliquen and Y. Forterre, A non-local rheology for dense granular flows, Philos. Trans. R. Soc. A **367**, 5091 (2009).
[17] P. Jop, V. Mansard, P. Chaudhuri, L. Bocquet, and A. Colin, Microscale Rheology of a Soft Glassy Material Close to Yielding, Phys. Rev. Lett. **108**, 148301 (2012).
[18] Q. Zhang and K. Kamrin, Microscopic Description of the Granular Fluidity Field in Nonlocal Flow Modeling, Phys. Rev. Lett. **118**, 058001 (2017).
[19] F. Radjai and S. Roux, Turbulentlike Fluctuations in Quasistatic Flow of Granular Media, Phys. Rev. Lett. **89**, 064302 (2002).
[20] A. L. Thomas, Z. Tang, K. E. Daniels, and N. M. Vriend, Force fluctuations at the transition from quasi-static to inertial granular flow, Soft Matter **15**, 8532 (2019).
[21] A. Santos, J. M. Montanero, J. W. Dufty, and J. J. Brey, Kinetic model for the hard-sphere fluid and solid, Phys. Rev. E **57**, 1644 (1998).
[22] O. Pouliquen, Velocity Correlations in Dense Granular Flows, Phys. Rev. Lett. **93**, 248001 (2004).
[23] J. Gaume, G. Chambon, and M. Naaim, Microscopic Origin of Nonlocal Rheology in Dense Granular Materials, Phys. Rev. Lett. **125**, 188001 (2020).
[24] E. DeGiuli, J. N. McElwaine, and M. Wyart, Phase diagram for inertial granular flows, Phys. Rev. E **94**, 012904 (2016).
[25] S. F. Edwards and R. B. S. Oakeshott, Theory of powders, Physica A **157**, 1080 (1989).
[26] S. Kim and K. Kamrin, Power-Law Scaling in Granular Rheology across Flow Geometries, Phys. Rev. Lett. **125**, 088002 (2020).
[27] E. Woldhuis, V. Chikkadi, M. S. van Deen, P. Schall, and M. van Hecke, Fluctuations in flows near jamming, Soft Matter **11**, 7024 (2015).

[28] Q. Xu, A. Singh, and H. M. Jaeger, Stress fluctuations and shear thickening in dense granular suspensions, J. Rheol. **64**, 321 (2020).
[29] O. Sedes, A. Singh, and J. F. Morris, Fluctuations at the onset of discontinuous shear thickening in a suspension, J. Rheol. **64**, 309 (2020).
[30] H. Perrin, M. Wyart, B. Metzger, and Y. Forterre, Nonlocal Effects Reflect the Jamming Criticality in Frictionless Granular Flows Down Inclines, Phys. Rev. Lett. **126**, 228002 (2021).
[31] P. E. Peyneau and J. N. Roux, Frictionless bead packs have macroscopic friction, but no dilatancy, Phys. Rev. E **78**, 011307 (2008).
[32] T. Kawasaki, D. Coslovich, A. Ikeda, and L. Berthier, Diverging viscosity and soft granular rheology in non-Brownian suspensions, Phys. Rev. E **91**, 012203 (2015).
[33] A. Favier de Coulomb, M. Bouzid, P. Claudin, E. Clément, and B. Andreotti, Rheology of granular flows across the transition from soft to rigid particles, Phys. Rev. Fluids **2**, 102301(R) (2017).
[34] I. Srivastava, L. E. Silbert, G. S. Grest, and J. B. Lechman, Flow-Arrest Transitions in Frictional Granular Matter, Phys. Rev. Lett. **122**, 048003 (2019).
[35] A. Singh, V. Magnanimo, K. Saitoh, and S. Luding, The role of gravity or pressure and contact stiffness in granular rheology, New J. Phys. **17**, 043028 (2015).
[36] N. Xu and C. S. O'Hern, Measurements of the yield stress in frictionless granular systems, Phys. Rev. E **73**, 061303 (2006).
[37] A. Taboada, N. Estrada, and F. Radjaï, Additive Decomposition of Shear Strength in Cohesive Granular Media from Grain-Scale Interactions, Phys. Rev. Lett. **97**, 098302 (2006).
[38] T. Hatano, Power-law friction in closely packed granular materials, Phys. Rev. E **75**, 060301(R) (2007).
[39] P. Olsson and S. Teitel, Critical Scaling of Shear Viscosity at the Jamming Transition, Phys. Rev. Lett. **99**, 178001 (2007).
[40] C. Heussinger, P. Chaudhuri, and J.-L. Barrat, Fluctuations and correlations during the shear flow of elastic particles near the jamming transition, Soft Matter **6**, 3050 (2010).
[41] Z. Shojaaee, J.-N. Roux, F. Chevoir, and D. E. Wolf, Shear flow of dense granular materials near smooth walls. I. Shear localization and constitutive laws in the boundary region, Phys. Rev. E **86**, 011301 (2012).
[42] P. Olsson and S. Teitel, Dynamic length scales in athermal, shear-driven jamming of frictionless disks in two dimensions, Phys. Rev. E **102**, 042906 (2020).
[43] Y. Forterre and O. Pouliquen, Flows of dense granular media, Annu. Rev. Fluid Mech. **40**, 1 (2008).
[44] M. Trulsson, B. Andreotti, and P. Claudin, Transition from the Viscous to Inertial Regime in Dense Suspensions, Phys. Rev. Lett. **109**, 118305 (2012).
[45] M. Bouzid, M. Trulsson, P. Claudin, E. Clément, and B. Andreotti, Nonlocal Rheology of Granular Flows across Yield Conditions, Phys. Rev. Lett. **111**, 238301 (2013).
[46] E. Azéma and F. Radjaï, Internal Structure of Inertial Granular Flows, Phys. Rev. Lett. **112**, 078001 (2014).
[47] E. DeGiuli, G. Düring, E. Lerner, and M. Wyart, Unified theory of inertial granular flows and non-Brownian suspensions, Phys. Rev. E **91**, 062206 (2015).
[48] L. E. Silbert, D. Ertas, G. S. Grest, T. C. Halsey, D. Levine, and S. J. Plimpton, Granular flow down an inclined plane: Bagnold scaling and rheology, Phys. Rev. E **64**, 051302 (2001).
[49] C. S. Campbell, Granular shear flows at the elastic limit, J. Fluid Mech. **465**, 261 (2002).
[50] S. Chialvo, J. Sun, and S. Sundaresan, Bridging the rheology of granular flows in three regimes, Phys. Rev. E **85**, 021305 (2012).
[51] D. Vescovi and S. Luding, Merging fluid and solid granular behavior, Soft Matter **12**, 8616 (2016).
[52] A. P. Santos, D. S. Bolintineanu, G. S. Grest, J. B. Lechman, S. J. Plimpton, I. Srivastava, and L. E. Silbert, Granular packings with sliding, rolling, and twisting friction, Phys. Rev. E **102**, 032903 (2020).
[53] F. Fazelpour, Z. Tang, and K. E. Daniels, The effect of grain shape and material on the nonlocal rheology of dense granular flows, Soft Matter **18**, 1435 (2022).
[54] P. V. Dsouza and P. R. Nott, Dilatancy-driven secondary flows in dense granular materials, J. Fluid Mech. **914**, A36 (2021).
[55] W. Shinoda, M. Shiga, and M. Mikami, Rapid estimation of elastic constants by molecular dynamics simulation under constant stress, Phys. Rev. B **69**, 134103 (2004).

[56] See Supplemental Material at http://link.aps.org/supplemental/10.1103/PhysRevFluids.7.084303 for details on the role of pressure damping and time step, as well as more fluctuation and coordination number data.
[57] S. J. Plimpton, Fast parallel algorithms for short-range molecular dynamics, J. Comput. Phys. **117**, 1 (1995).
[58] A. P. Thompson, H. M. Aktulga, R. Berger, D. S. Bolintineanu, W. M. Brown, P. S. Crozier, P. J. in 't Veld, A. Kohlmeyer, S. G. Moore, T. D. Nguyen, R. Shan, M. J. Stevens, J. Tranchida, C. Trott, and S. J. Plimpton, LAMMPS-A flexible simulation tool for particle-based materials modeling at the atomic, meso, and continuum scales, Comput. Phys. Commun. **271**, 108171 (2022).
[59] H. Flyvbjerg and H. G. Petersen, Error estimates on averages of correlated data, J. Chem. Phys. **91**, 461 (1989).
[60] G. G. Giusteri and R. Seto, A theoretical framework for steady-state rheometry in generic flow conditions, J. Rheol. **62**, 713 (2018).
[61] É. Guazzelli and O. Pouliquen, Rheology of dense granular suspensions, J. Fluid Mech. **852**, P1 (2018).
[62] D. Fenistein, J.-W. van de Meent, and M. van Hecke, Core Precession and Global Modes in Granular Bulk Flow, Phys. Rev. Lett. **96**, 118001 (2006).
[63] L. E. Silbert, Temporally Heterogeneous Dynamics in Granular Flows, Phys. Rev. Lett. **94**, 098002 (2005).
[64] É. Couturier, F. Boyer, O. Pouliquen, and É. Guazzelli, Suspensions in a tilted trough: Second normal stress difference, J. Fluid Mech. **686**, 26 (2011).
[65] D. Lootens, H. Van Damme, and P. Hébraud, Giant Stress Fluctuations at the Jamming Transition, Phys. Rev. Lett. **90**, 178301 (2003).
[66] R. L. Hoffman, Discontinuous and dilatant viscosity behavior in concentrated suspensions. I. Observation of a flow instability, Trans. Soc. Rheol. **16**, 155 (1972).
[67] F. Radjai, J.-Y. Delenne, E. Azéma, and S. Roux, Fabric evolution and accessible geometrical states in granular materials, Granul. Matter **14**, 259 (2012).
[68] I. Srivastava, J. B. Lechman, G. S. Grest, and L. E. Silbert, Evolution of internal granular structure at the flow-arrest transition, Granul. Matter **22**, 41 (2020).
[69] D. Vescovi, D. Berzi, and C. di Prisco, Fluid–solid transition in unsteady, homogeneous, granular shear flows, Granul. Matter **20**, 27 (2018).
[70] M. L. Goff, E. Bertin, and K. Martens, Giant fluctuations in the flow of fluidised soft glassy materials: An elasto-plastic modelling approach, J. Phys. Mater. **3**, 025010 (2020).
[71] J. T. Clemmer, K. M. Salerno, and M. O. Robbins, Criticality in sheared, disordered solids. I. Rate effects in stress and diffusion, Phys. Rev. E **103**, 042605 (2021).
[72] C. S. O'Hern, L. E. Silbert, A. J. Liu, and S. R. Nagel, Jamming at zero temperature and zero applied stress: The epitome of disorder, Phys. Rev. E **68**, 011306 (2003).
[73] T. P. C. van Noije, M. H. Ernst, R. Brito, and J. A. G. Orza, Mesoscopic Theory of Granular Fluids, Phys. Rev. Lett. **79**, 411 (1997).